

1 **Theoretical Framework for Measuring Cloud Effective**
2 **Supersaturation Fluctuations with an Advanced Optical System**

3 Ye Kuang¹, Jiangchuan Tao¹, Hanbing Xu², Li Liu³, Pengfei Liu⁴, Wanyun Xu⁵, Weiqi Xu⁶, Yele Sun⁶,
4 Chunsheng Zhao⁷

5 ¹ Institute for Environmental and Climate Research, College of Environment and Climate, Jinan
6 University, Guangzhou, Guangdong, China

7 ² Experimental Teaching Center, Sun Yat-Sen University, Guangzhou, China

8 ³ Key Laboratory of Regional Numerical Weather Prediction, Institute of Tropical and Marine
9 Meteorology, China Meteorological Administration, Guangzhou, China.

10 ⁴ School of Earth and Atmospheric Sciences, Georgia Institute of Technology, Atlanta, GA, USA

11 ⁵ State Key Laboratory of Severe Weather, Key Laboratory for Atmospheric Chemistry, Institute of
12 Atmospheric Composition, Chinese Academy of Meteorological Sciences, Beijing, China

13 ⁶ State Key Laboratory of Atmospheric Boundary Layer Physics and Atmospheric Chemistry, Institute
14 of Atmospheric Physics, Chinese Academy of Sciences, Beijing, China.

15 ⁷ Department of Atmospheric and Oceanic Sciences, School of Physics, Peking University, Beijing,
16 China.

17

18 Correspondence: Ye Kuang (kuangye@jnu.edu.cn)

19

20

21

22

23

24

25

26

27

28

29

30

31 **Abstract**

32 Supersaturation is crucial in cloud physics, determining aerosol activation and influencing cloud
33 droplet size distributions, yet its measurement remains challenging and poorly constrained. This study
34 proposes a theoretical framework to simultaneously observe critical activation diameter and
35 hygroscopicity of activated aerosols through direct measurements of scattering and water induced
36 scattering enhancement of interstitial and activated aerosols, enabling effective supersaturation
37 measurements. Advanced optical systems based on this framework allows minute- to second-level
38 effective supersaturation measurements, capturing fluctuations vital to cloud microphysics. Although
39 currently limited to clouds with supersaturations below $\sim 0.2\%$ due to small scattering signals from
40 sub-100 nm aerosols, advancements in optical sensors could extend its applicability. Its suitability for
41 long-term measurements allows for climatological studies of fogs and mountain clouds. When
42 equipped with aerial vehicles, the system could also measure aloft clouds. Therefore, the proposed
43 theory serving a valuable way for both short-term and long-term cloud microphysics and aerosol-cloud
44 interaction studies.

45

46

47

48

49

50

51

52

53

54

55

56

57

58

59 **1. Introduction**

60 Clouds and fogs play critical roles in weather patterns and climate change, influencing both
61 precipitation and the radiative balance of the Earth's atmosphere. As such, they are central to accurate
62 weather and climate predictions. Despite their importance, representing clouds accurately in
63 atmospheric models remains a significant challenge (Seinfeld and Pandis, 2016) . Supersaturation,
64 defined as the difference between the actual water vapor pressure (e) and the saturation vapor pressure
65 (e_s) which is typically expressed as a dimensionless quantity $(e - e_s)/e_s$, is a key parameter that links
66 aerosols to clouds through the process of aerosol activation, making it fundamental to cloud physics
67 (Seinfeld and Pandis, 2016). Despite its importance, supersaturation is difficult to measure and remains
68 poorly understood and constrained (Yang et al., 2019). Previous studies have highlighted that other
69 than the mean supersaturation, supersaturation fluctuations also play critical roles in aerosol activation
70 and cloud droplet growth, ultimately influencing the evolution of cloud droplet size distributions
71 (Kaufman and Tanré, 1994;Sardina et al., 2015;Chandrakar et al., 2018;Chandrakar et al., 2020;Shaw
72 et al., 2020). For instance, cloud chamber experiments have shown that supersaturation fluctuations
73 promote aerosol activation and enhance aerosol activity (Shawon et al., 2021;Anderson et al., 2023),
74 particularly when the magnitude of these fluctuations is comparable to the mean supersaturation
75 (Prabhakaran et al., 2020). Both experimental and theoretical analyses suggest that supersaturation
76 fluctuations can broaden cloud droplet size distributions (Chandrakar et al., 2016;Abade et al.,
77 2018;Saito et al., 2019).

78 Supersaturation fluctuations arise not only from turbulent variations in the temperature and vapor
79 pressure fields but also from the growth and evaporation of droplets, which drive mass and heat
80 exchange between droplets and the surrounding air. As noted by Shaw et al. (2020), measuring
81 supersaturation remains a formidable challenge due to its extreme sensitivity to variations in water
82 vapor pressure and temperature. Although current techniques of water vapor and temperature
83 measurements could not achieve accurately measurements of supersaturation, however, direct
84 measurements of water vapor pressure and temperature were previously used to estimate
85 supersaturation fluctuations, and obtained results have demonstrated that the supersaturation is indeed
86 a fluctuating quantity (Ditas et al., 2012;Siebert and Shaw, 2017).. Currently, cloud and fog
87 supersaturation are typically retrieved from aerosol activation measurements (Ditas et al., 2012) or
88 estimated from vertical velocity measurements and droplet size distribution measurements (Siebert
89 and Shaw, 2017;Cooper, 1989). Supersaturation parameterizations based on vertical velocity are
90 common in models (Abdul-Razzak et al., 1998), while field measurements often rely on aerosol

91 activation data to investigate supersaturation fluctuations and evolutions in clouds and fogs (Ditas et
92 al., 2012;Hammer et al., 2014;Shen et al., 2018;Mazoyer et al., 2019;Zíková et al., 2020;Wainwright
93 et al., 2021;Kuang et al., 2024). In addition, supersaturations were also estimated using the closure
94 between cloud droplet number and cloud condensation nuclei (CCN) measurements at various
95 supersaturations (Yum et al., 1998;Sanchez et al., 2016;Sanchez et al., 2021;Saliba et al., 2023).

96 In summary, direct measurements of water vapor pressure and temperature are essential for
97 quantifying supersaturations; however, they are nearly impossible with current technologies.
98 Supersaturation measurements from aerosol and cloud microphysics monitoring often reflect an
99 effective supersaturation that drives aerosol activation, which is indeed critical in cloud physics. The
100 complexity of cloud formation and evolution and the central role of supersaturation in these processes
101 underscore the need for precise measurement and representation of supersaturation. Advancements in
102 measuring and understanding supersaturation are essential for improving the accuracy of models and
103 reducing uncertainties in weather and climate predictions. In this study, we propose a theoretical
104 framework for using optical methods to observe effective supersaturations based on aerosol activation
105 in clouds and preliminarily validated utilizing data obtained from field campaigns. The feasibility of
106 employing an advanced optical system to measure supersaturation fluctuations were also explored and
107 discussed.

108 **2. Methods and Materials**

109 **2.1 Observing effective supersaturations on the basis of κ -Köhler theory**

110 The concept of effective supersaturation was introduced based on aerosol activation
111 measurements (Hudson and Yum, 1997;Hudson et al., 2010), which could be defined as the
112 supersaturation in CCN chamber (CCN activation under constant supersaturation conditions) that
113 resulted in the same aerosol activation fraction with the observed aerosol activation fraction in clouds.
114 Quick fluctuations in supersaturation would result in the effective supersaturation, which directly
115 determined by aerosol activation, differs from the mean supersaturation which is determined by
116 average water vapor content and temperature. However, the concept of κ -Köhler theory is established
117 according to a constant supersaturation scenario, therefore provides a framework for deriving effective
118 supersaturation from aerosol activation measurements in clouds (Petters and Kreidenweis, 2007):

$$119 \quad S = \frac{D^3 - D_d^3}{D^3 - D_d^3(1 - \kappa)} \cdot \exp\left(\frac{4\sigma_s/a \cdot M_{water}}{R \cdot T \cdot D_p \cdot g \cdot \rho_w}\right) \quad (1)$$

120 where S is the saturation ratio over an aqueous solution droplet with a diameter of D , D_d is the dry
121 diameter, $\sigma_{s/a}$ is the surface tension of solution/air interface, T is the temperature, M_{water} is the
122 molecular weight of water, R is the universal gas constant, ρ_w is the density of water, and κ is the
123 hygroscopicity parameter. The κ -Köhler theory tells that if the critical diameter of aerosol activation
124 (D_a) and corresponding aerosol hygroscopicity parameter κ are known, the surrounding
125 supersaturation can be retrieved based on air temperature measurements and by assuming $\sigma_{s/a}$ the
126 surface tension of water (as shown in Fig.S1a). Note that D_a and κ are not independent with each other,
127 average κ of aerosols with diameter D_a is needed. Previous studies have shown that the reduction in
128 surface tension (Nozière et al., 2010;Gérard et al., 2016;Ovadnevaite et al., 2017) associated with
129 surfactants in atmospheric aerosols can affect aerosol activation and, consequently, the derivation of
130 effective supersaturation. However, if the derivation of κ (as done in this study) assumes a constant
131 water surface tension, the impact of surface tension changes is minimized, as these effects are already
132 incorporated in the κ calculation. Nonetheless, differences in surface tension between supersaturated
133 and subsaturated conditions (Davies et al., 2019;Petters and Kreidenweis, 2013;Liu et al., 2018), and
134 their impact on effective supersaturation, still exist. Additionally, prior research has suggested that
135 slightly soluble components in aerosols can influence κ values under both supersaturated and
136 subsaturated conditions (Ho et al., 2010;Petters and Kreidenweis, 2008;Lee et al., 2022;Han et al.,
137 2022;Riipinen et al., 2015;Wang et al., 2019;Whitehead et al., 2014). Therefore, κ observed under
138 subsaturated conditions would affect the derivation of effective supersaturation.

139 However, the simultaneous measurements of D_a and κ of activated aerosols with diameters
140 around D_a are indeed challenging. The direct measurements of size-resolved activation ratio (AR) in
141 clouds are essential for D_a retrievals through the following equation:

$$142 \quad AR(D_p) = \frac{MAF}{2} \left(1 + \operatorname{erf} \left(\frac{D_p - D_a}{\sqrt{2\pi}\sigma} \right) \right) \quad (2)$$

143 Where D_p is the particle diameter, MAF is the maximum activation fraction and D_a is critical
144 activation diameter, σ is associated with the slope of the size-resolved AR curve near D_a and mostly
145 influenced by the heterogeneous distribution of aerosols near D_a as well as supersaturation fluctuations
146 (note that not effective supersaturation fluctuations). This formula was previously proposed by Rose
147 et al. (2008) to fit the AR measurements and widely used in AR parameterizations (Tao et al., 2018b).
148 Therefore, it typically requires a unique inlet system and a suite of instruments that measure the aerosol
149 size distribution of both interstitial and total aerosol populations (Hammer et al., 2014;Zíková et al.,

150 2020). Consequently, this is rarely done, even in ground fog measurements. Instead, D_a was usually
151 estimated from aerosol measurements and fog droplet size distributions measurements which
152 indirectly provides the number concentrations of activated aerosols therefore could be used in
153 retrieving D_a through assuming that all aerosols larger than D_a are activated (Mazoyer et al.,
154 2019;Wainwright et al., 2021;Shen et al., 2018) which brings uncertainty in D_a derivations due to that
155 not all aerosols larger than D_a are activated, because the MAF in Eq.2 does not equal to unit although
156 usually very close to (Tao et al., 2018b). For the effective supersaturation measured in aloft clouds,
157 the aerosol number size distributions inside and outside the cloud as well as cloud droplet number
158 concentrations were used by Ditas et al. (2012) to derive D_a , and other approaches were also used
159 (Gong et al., 2023). The κ values were usually retrieved from size-resolved cloud condensation nuclei
160 measurements under certain supersaturations (Hammer et al., 2014;Mazoyer et al., 2019) or from
161 growth factor measurements (Wainwright et al., 2021) or sometime assumed due to the lack of
162 measurements. The κ of activated aerosols were not directly measured in these studies due to the
163 difficulty of the direct sampling of activated aerosols as well as subsequent hygroscopicity
164 measurements.

165 Two types of supersaturation fluctuations have been previously identified. The first type involves
166 fluctuations in supersaturation directly governed by water vapor pressure and temperature, as
167 described by Siebert and Shaw (2017). These fluctuations are linked to turbulence and water phase
168 changes that influence water vapor pressure and temperature. The second type concerns fluctuations
169 in effective supersaturation, which are associated with the activation and deactivation processes of
170 aerosols, as noted by Ditas et al. (2012). The first type of fluctuations dictates the instantaneous growth
171 and evaporation of droplets, thereby controlling the activation and deactivation of cloud droplets. As
172 such, the second type of fluctuation is inherently driven by the first type. The theoretical framework
173 proposed in this study enables the measurement of fluctuations in effective supersaturation.

174

175 **2.2 Field measurements**

176 Kuang et al. [2024] developed an advanced aerosol-cloud sampling system designed to measure
177 fog and cloud activation processes. This compact, integrated system can automatically switch between
178 different inlets, including PM_{10} (particles and droplets with an aerodynamic diameter $< 10 \mu m$), $PM_{2.5}$
179 (particles and droplets with an aerodynamic diameter $< 2.5 \mu m$) impactor, and Total Suspended
180 Particles (TSP, encompassing all particles and droplets) (as shown in Fig. S2). When combined with

181 instruments that measure aerosol physical, optical, and chemical properties, this system is well-suited
182 for investigating cloud microphysics and chemistry. It was utilized in the AQ-SOFAR campaign,
183 dedicated to studying AQueous Secondary aerOsol formation in Fogs and Aerosols and their Radiative
184 effects in the North China Plain (Kuang et al., 2024).

185 During this campaign, several radiation fog events were observed, enabling the measurement of
186 size-resolved AR curves, aerosol hygroscopicity as well as chemical compositions of interstitial and
187 activated aerosols within fogs. These measurements provided insights into the evolution of
188 supersaturations (Kuang et al., 2024). Notably, aerosol hygroscopicity was determined using a
189 humidified nephelometer system, located downstream of the inlet system. This system measured
190 multiwavelength scattering coefficients (450 nm, 525 nm, 635 nm) under both nearly dry ($RH < 20\%$)
191 and humid conditions ($RH \sim 84\%$), offering aerosol hygroscopicity data based on the optical theory
192 proposed by Kuang et al. (2017). The size-resolved AR curves and aerosol chemical compositions
193 were obtained through the aerosol size distribution and the aerosol mass spectrometry measurements
194 downstream of the inlet system. A schematic of the inlet system and associated instruments is provided
195 in Fig. S1. Further details about the entire experimental setup, size-resolved AR calculations as well
196 as data analysis about mass spectrometer measurements can be found in Kuang et al. (2024).

197 In addition, the particle number size distributions (PNSDs) in dry state, which range from about
198 10 nm to 10 μm , were jointly measured by a Twin Differential Mobility Particle Sizer (TDMPS,
199 Leibniz-Institute for Tropospheric Research, Germany) or a scanning mobility particle size
200 spectrometer (SMPS) and an Aerodynamic Particle Sizer (APS, TSI Inc., Model 3321) in six field
201 campaigns conducted on the North China Plain which are detailed in Kuang et al. (2018). The mass
202 concentrations of black carbon (BC) were measured using a Multi-Angle Absorption Photometer
203 (MAAP Model 5012, Thermo, Inc., Waltham, MA USA) or an aethalometer (AE33) (Drinovec et al.,
204 2015) in these field campaigns. Details about these measurements and quality assurance was
205 introduced in Kuang et al. (2018).

206 **2.3 Method of simulating scattering coefficients of interstitial aerosols and activated aerosols**

207 For each paired PNSD and BC mass concentration, the size distribution of dry-state PM_{10} was
208 obtained using the following formula (the penetration curve shape from Gussman et al. (2002) was
209 also included for considering the non-ideality cutoff of the impactor, and assuming aerosol density of
210 1.6 g/cm^3 for converting aerodynamic diameter to mobility diameter) :

211 $\text{PNSD}(D_p)_{PM_1} = \text{PNSD}(D_p) \times R(D_p)$ (3)

212 Where $R(D_p)$ is the penetration ratio of aerosols as a function of particle diameter D_p of the PM_1
 213 impactor. Further, $\text{PNSD}(D_p)_{PM_1}$ and the BC mass concentration was used to simulate the size-
 214 resolved aerosol scattering coefficients ($d\sigma_{sp}/d\log D_p$) at 450 nm, 525 nm and 636 nm that is
 215 consistent with the angular truncation and light source nonideality of Auora 3000 nephelometer
 216 (Müller et al., 2011), where σ_{sp} represents aerosol scattering coefficient. In this Mie calculation, the
 217 shape of black carbon mass size distributions are consistent with the one used in simulations of Kuang
 218 et al. (2017) assuming fractions of BC mass that are externally mixed is 0.5. Details about the Mie
 219 theory calculations can also be found in Ma et al. (2011) and Kuang et al. (2017).

220 With given size-resolved AR curve that produced using Eq.2, the size-resolved aerosol scattering
 221 coefficients of interstitial aerosols can be calculated using the following formula:

222 $d\sigma_{sp,inter}/d\log D_p(D_p) = d\sigma_{sp}/d\log D_p(D_p) \times (1 - AR(D_p))$ (4)

223 The size-resolved aerosol scattering coefficients of activated aerosols can be calculated using:

224 $d\sigma_{sp,act}/d\log D_p(D_p) = d\sigma_{sp}/d\log D_p(D_p) - d\sigma_{sp,inter}/d\log D_p(D_p)$ (5)

225 Scattering coefficients of total aerosol populations (interstitial plus activated) and interstitial aerosols
 226 can be derived through integration of $d\sigma_{sp}/d\log D_p(D_p)$ and $d\sigma_{sp,inter}/d\log D_p(D_p)$.

227

228 **3. Theoretical Framework and Concept Design of the Advanced Optical System**

229 **3.1 Theory of Observing Critical Activation Diameter Using Scattering Measurements**

230 The typical shape of size-resolved AR curves observed in atmospheric fogs and clouds is
 231 illustrated in Fig. 1a (Ditas et al., 2012; Hammer et al., 2014; Zíková et al., 2020; Wainwright et al.,
 232 2021; Kuang et al., 2024). In clouds, aerosols can be classified as either activated aerosols, which form
 233 cloud droplets, or inactivated aerosols, which remain as interstitial aerosols. The critical diameter that
 234 distinguishes interstitial aerosols from cloud or fog droplets varies depending on the supersaturation
 235 (Kuang et al., 2024). A diameter of 2.5 μm is typically suitable for surface fogs with relatively lower
 236 supersaturations ($<0.1\%$), while 1 μm is more appropriate for aloft clouds with higher supersaturations
 237 ($>0.1\%$) (Mazoyer et al., 2019; Kuang et al., 2024; Lu et al., 2020). The typical AR curve shows that
 238 most aerosols larger than D_a are activated, while most smaller aerosols remain inactivated. As a result,

239 the scattering properties, such as size-resolved scattering coefficients (Fig. 1a), the scattering Ångström
 240 exponent (SAE) and its wavelength dependence, which are directly related to aerosol size distribution,
 241 differ significantly between interstitial and activated aerosols.

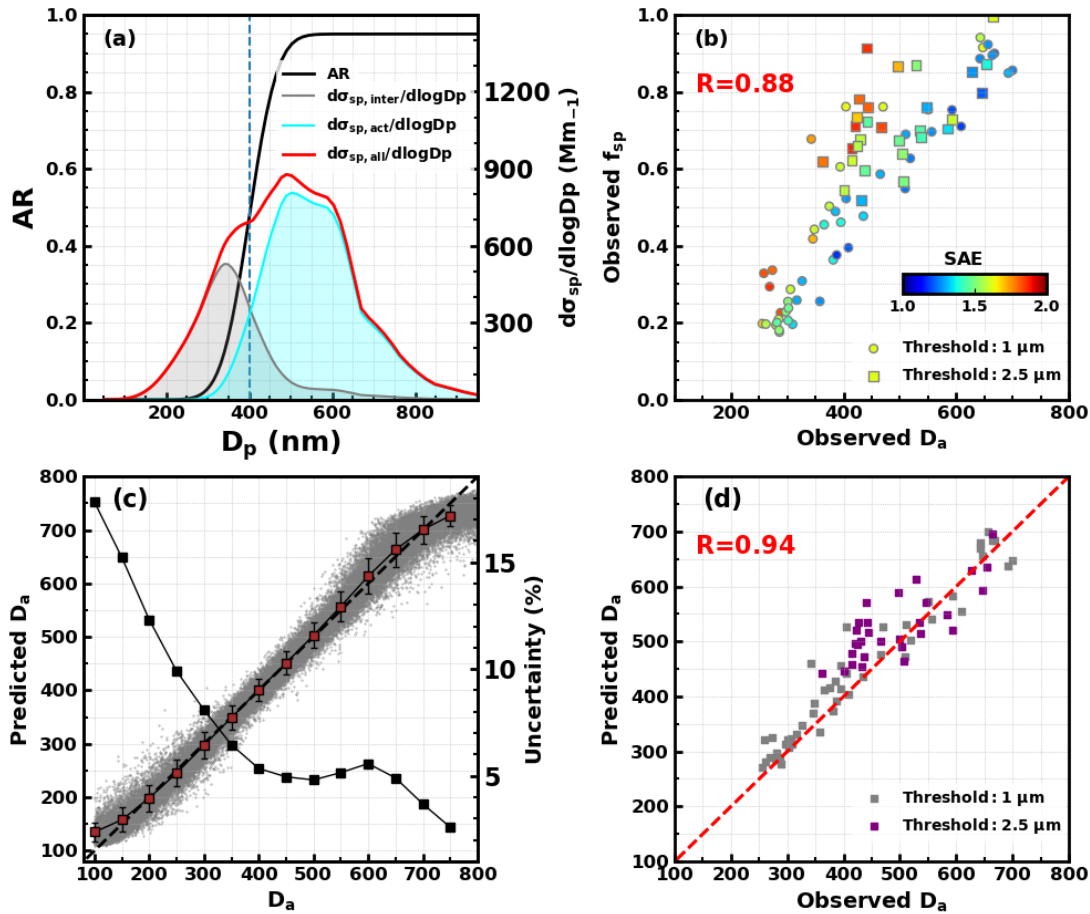


Figure 1. (a) The typical shape of size-resolved aerosol activation ratio (AR) curve produced using the function of Eq.2, with the D_a of 400 nm, the MAF of 0.95 and the σ of 30 (as an example). The average PNSD observed in the North China Plain from six campaigns as introduced in Sect2.2 and the example AR curve was used to simulate an example of the size-resolved aerosol scattering (σ_{sp}) distributions of interstitial and activated aerosols at 525 nm; (b) Relations between observed D_a and f_{sp} during the AQ-SOFAR campaign using 1 and 2.5 μm as the threshold of interstitial aerosols, with the scatter points are colored with corresponding SAE of total dry state PM_{10} aerosols. (c) Comparisons of all prescribed D_a and predicted D_a values represented by scatter points, they are further binned with interval of 50 nm, averages and standard deviations represented by purple squares and their error bars, black squares represent relative uncertainty of the right axis at each bin; (d) The comparisons of D_a retrieved using activation ratio observations and those predicted using scattering observations as inputs of the trained model, dashed lines represent 1:1 lines.

242 If we focus on PM_{10} of the total dry aerosol population (the reasoning for this is discussed in Sect.
 243 S1 of the supplement), the scattering fraction of interstitial aerosols in the total dry PM_{10} population,
 244 defined as $f_{sp} = \sigma_{sp,PM_{10},inter}(dry, 525 \text{ nm}) / \sigma_{sp,PM_{10},all}(dry, 525 \text{ nm})$, where
 245 $\sigma_{sp,PM_{10},inter}(dry, 525 \text{ nm})$ is the scattering coefficient of PM_{10} interstitial aerosols in a dry state at a
 246 wavelength of 525 nm, and $\sigma_{sp,PM_{10},all}(dry, 525 \text{ nm})$ is that of all PM_{10} aerosols, is likely to be highly

247 correlated with D_a . Generally, the larger the D_a , the higher the f_{sp} . This relationship was directly
248 confirmed using D_a and the scattering properties of dry PM₁ interstitial and total aerosols during the
249 AQ-SOFAR campaign, as shown in Fig. 1b, that observed D_a correlates highly with observed f_{sp}
250 (R=0.88). However, at a given D_a , f_{sp} can vary significantly, and these variations are closely related
251 to the SAE of all dry PM₁ aerosols, which are mainly determined by aerosol size distribution. In fact,
252 aside from the size distribution of the total aerosol population that determines SAE, the shape of the
253 AR curve also plays a significant role in the variations of f_{sp} .

254 The nephelometer measures the aerosol scattering coefficient at three wavelengths, enabling
255 direct measurements of the SAE for both the total dry-state PM₁ aerosols and the interstitial aerosols.
256 Therefore, the relationship between f_{sp} and D_a can be further constrained by the SAE of interstitial
257 and activated aerosols, as well as their wavelength dependence. This implies that a simple formulaic
258 relationship between f_{sp} and D_a may not exist. However, the six scattering parameters
259 $\sigma_{sp,PM_1,inter}(dry, \lambda)$ —at 450 nm, 525 nm, 635 nm, and $\sigma_{sp,PM_1,all}(dry, \lambda)$ at 450 nm, 525 nm, 635
260 nm—contain both the f_{sp} information and the SAE characteristics of both aerosol groups, thus
261 potentially be used to accurately retrieve D_a . Machine learning techniques, which are well-suited for
262 handling complex relationships, can be applied to this problem.

263 This assumption was tested using Mie theory, based on aerosol size distributions sampled during
264 six campaigns conducted in the North China Plain region (Kuang et al., 2018). For each aerosol size
265 distribution, we randomly assumed different activation curves using Eq.2. That is, for each PNSD from
266 those campaigns, the scattering coefficients of submicron interstitial and activated+interstitial aerosols
267 at wavelengths of 450 nm, 525 nm and 635 nm corresponding to nephelometer case under 100 size-
268 resolved AR scenarios were simulated using the procedure. And each size-resolved AR curve was
269 produced by using randomly produced D_a , σ and MAF as inputs of Eq.2. In the random step, the
270 range of D_a is 100-700 nm, the range of σ is 1-30, the range of MAF is 0.5-1. In each pair, simulated
271 $\sigma_{sp,PM_1,inter}(dry, \lambda)$ —at 450 nm, 525 nm, 635 nm, and $\sigma_{sp,PM_1,all}(dry, \lambda)$ at 450 nm, 525 nm, 635
272 nm was the x values of the random forest model, corresponding D_a is the y value of the random forest
273 model, and the random forest package from Python Scikit-Learn machine learning library
274 (<http://scikit-learn.org/stable/index.html>) is used for this purpose. With these configurations, more
275 than million pairs are simulated. To preliminarily validate this approach, we randomly selected 75%
276 of the simulated data pairs for training the model, while the remaining 25% were used for validation.

277 The results, shown in Fig. 1c, indicate that this approach could retrieve D_a with an uncertainty of
 278 less than 10% for D_a larger than 250 nm, and even as low as ~6% for D_a larger than 350 nm. However,
 279 the uncertainty increases as D_a decreases, particularly for D_a smaller than 250 nm. The larger
 280 uncertainty at smaller D_a is since aerosols smaller than 250 nm typically contribute less than 10% to
 281 total scattering in the dry state, making f_{sp} less sensitive to variations in D_a . This issue becomes more
 282 pronounced when D_a is less than 100 nm, as aerosols smaller than 150 nm generally contribute
 283 negligibly to total aerosol scattering [Kuang et al., 2018]. This method was further validated using
 284 observations from the AQ-SOFAR campaign. In this validation, D_a values were first predicted using
 285 aerosol scattering observations with the trained model and then compared with D_a values retrieved
 286 from size-resolved AR measurements, as shown in Fig. 1d. It should be noted that the impactor
 287 operates in a sequence of PM₁, PM_{2.5}, TSP, and then back to PM₁, with the flow alternating between
 288 a thermodenuder and bypass every 10 minutes for each inlet. To calculate size-resolved AR curves,
 289 we assumed that aerosol populations remained unchanged during the 30-minute period (based on
 290 comparisons between PM₁/PM_{2.5} and TSP inlets), which can sometimes introduce significant
 291 uncertainties in the size-resolved AR calculations. When using PM_{2.5} as the threshold, the much lower
 292 number concentrations of aerosols larger than 400 nm can introduce more uncertainty in D_a retrievals,
 293 partially explaining the lower performance in Fig. 1d when using the PM_{2.5} threshold.

294 3.2 Method of observing Hygroscopicity of Activated Aerosols

295 Measuring the hygroscopicity κ of activated aerosols at the critical activation diameter D_a under
 296 varying supersaturations is challenging, not only due to technical limitations but also because of the
 297 inherent variability in D_a . Kuang et al. (2017) introduced a novel optical method for observing aerosol
 298 hygroscopicity by using the aerosol light scattering enhancement factor $f(RH)$ that associated with
 299 aerosol hygroscopic growth. This method is particularly suitable for the objectives outlined here. The
 300 method requires SAE and light scattering enhancement factors $f(RH)$ of activated aerosols as inputs,
 301 and retrieved κ can be termed as $\kappa_{act,f(RH)}$ which represents the overall hygroscopicity of activated
 302 aerosols and can be understood as the average κ of activated aerosols with the scattering contribution
 303 of each aerosol particle as the weight (Kuang et al., 2020). The scattering coefficients of activated
 304 aerosols at multiwavelength can be calculated as $\sigma_{sp,PM_{1,act}}(dry, \lambda) = \sigma_{sp,PM_{1,all}}(dry, \lambda) -$
 305 $\sigma_{sp,PM_{1,inter}}(dry, \lambda)$, therefore corresponding SAE can be obtained. The $f(RH)$ of activated aerosols
 306 at 525 nm can be calculated as the following:

$$f(RH)_{act} = \frac{\sigma_{sp,PM_{1,all}}(RH,525\text{ nm}) - \sigma_{sp,PM_{1,inter}}(RH,525\text{ nm})}{\sigma_{sp,PM_{1,all}}(dry,525\text{ nm}) - \sigma_{sp,PM_{1,inter}}(dry,525\text{ nm})} \quad (6)$$

During the AQ-SOFAR campaign, a humidified nephelometer system consisting of two nephelometers—one measuring aerosol scattering in the dry state and the other at a fixed RH of 84%—was placed downstream of the PM₁ impactor. This setup allows for the humidification of dry-state interstitial aerosols and total aerosol populations to a high RH (e.g., above 80%), facilitating the required measurements, therefore severs one choice. The Retrieved $\kappa_{act,f(RH)}$ under different D_a conditions are shown in Fig.2a, demonstrating significant variations in $\kappa_{act,f(RH)}$ and its variations need to be constrained. Also, the derived $\kappa_{act,f(RH)}$ are compared to those estimated from aerosol chemical composition measurements ($\kappa_{act,chem}$, details about calculation methods can refer to Kuang et al. (2020)), as shown in Fig.2b and in general agree. Note that the mass spectrometer could not identify

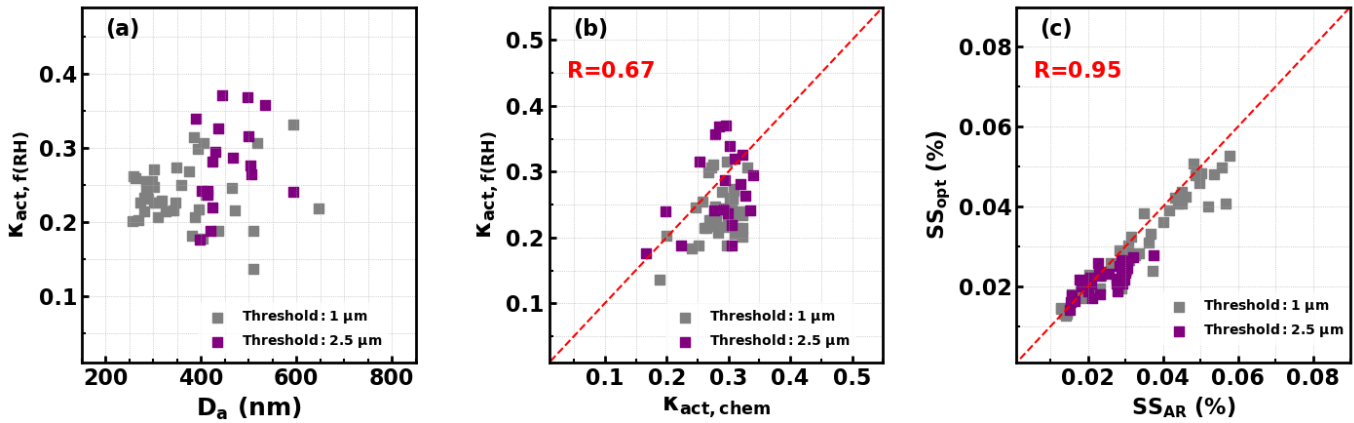


Figure 2. (a) Retrieved $\kappa_{act,f(RH)}$ under different D_a conditions; (b) Comparison between κ of activated aerosols retrieved from the optical method ($\kappa_{act,f(RH)}$) and estimated from aerosol chemical composition measurements ($\kappa_{act,chem}$); (c) Comparisons between effective supersaturations (SSs) derived from size-resolved AR measurements as well as $\kappa_{act,chem}$ (SS_{AR}) and from the optical measurements (SS_{opt}). Dashed red lines represent 1:1.

all aerosol components, and assumptions about the mixing rule as well as densities of components would bring uncertainties (Kuang et al., 2021). The comparisons between effective supersaturations derived from size-resolved AR measurements as well as $\kappa_{act,chem}$ and from the optical method are shown in Fig.2c. On average, 0.002% of SS bias are observed due to the bias of D_a which associated more with assumptions made in D_a retrievals as previously discussed. As demonstrated by Kuang et al. (2024), for the fog case in the campaign, the threshold of 2.5 μm should be used, however, does not affect the comparisons here.

Qiao et al. (2024) developed an advanced outdoor nephelometer system that measures aerosol dry scattering coefficients and scattering coefficients at nearly ambient RH without the need for

326 humidifying the sample air by placing the entire nephelometer system in ambient air, with the
 327 instruments protected by a specially designed enclosure. This innovative design offers new insights
 328 into the hygroscopicity measurements of activated aerosols. Under cloud conditions, where the
 329 ambient RH is close to 100%, aerosol scattering under subsaturated conditions can be measured
 330 directly by applying heater.

331 3.3 Concept Design of the Advanced Optical System for Measuring Effective 332 Supersaturations

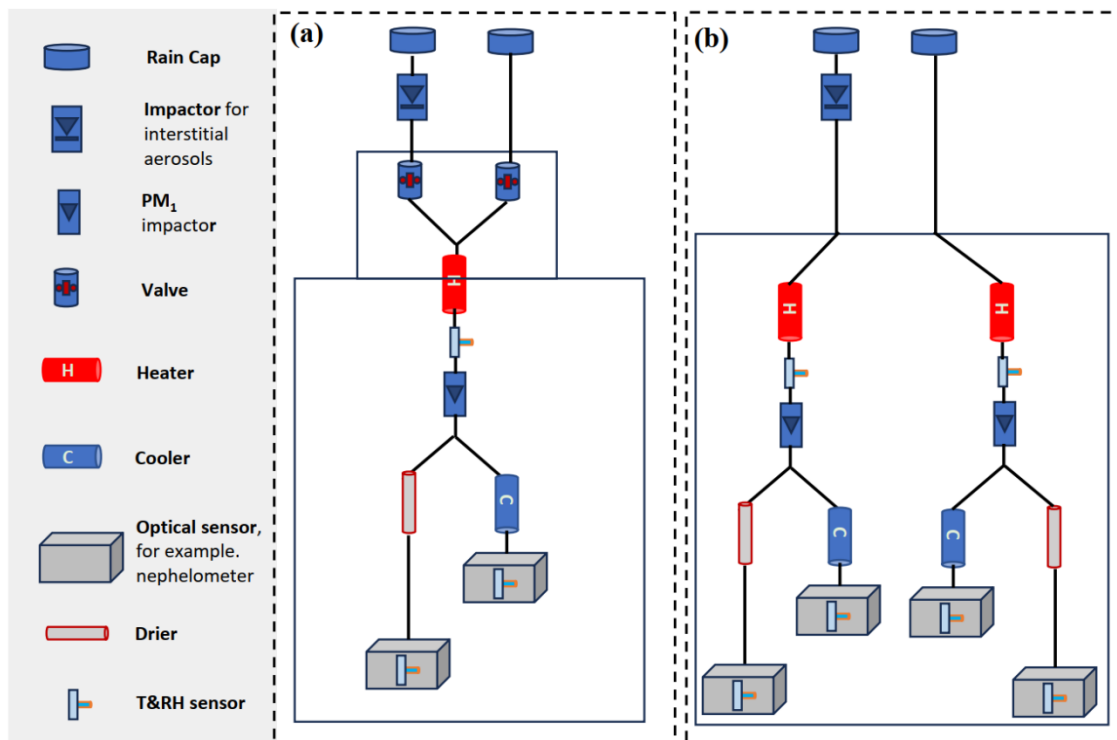


Figure 3. Concept design of the advanced optical system with different number of optical sensors, (a) using two nephelometers or other optical sensors; (b) using four nephelometers or other optical sensors. The heater upstream of the sample is used to reduce the relative humidity (RH) to below 60%, ensuring the evaporation of most of the water content, to make sure the consistency of needed PM₁ cut. The cooler upstream of the 'wet' nephelometer increases the sample RH to approximately 90%, allowing hygroscopicity measurements under conditions close to supersaturation.

333 Based on the proposed optical methods for measuring D_a and $\kappa_{act,f(RH)}$, a conceptual design for
 334 outdoor instruments capable of measuring effective supersaturation with relatively high time
 335 resolution can be envisioned, as shown in Fig. 3a. The aerosol-cloud sampling system includes two
 336 inlets: one equipped with a PM₁ or PM_{2.5} impactor (depending on cloud type) to sample interstitial
 337 aerosols, and another with a TSP inlet to sample both interstitial aerosols and cloud/fog droplets. A
 338 PM₁ impactor is placed downstream of the inlet system, where the RH of the sample air is reduced to
 339 70% (as discussed in Sect. S1 of the manuscript) through heater. Downstream of the PM1 impactor,

340 the sample flow is split into two streams: one is further dried to an RH below 10% before aerosol
341 scattering coefficients are measured by the “dry” nephelometer, and the other is passed through an
342 intelligent cooler to ensure the sample RH in the “wet” nephelometer remains close to 90%. The
343 sample air is automatically switched between the interstitial inlet and the TSP inlet at set intervals,
344 such as one minute for each inlet, enabling minute-level measurements of effective supersaturations.
345 While the nephelometer can output scattering measurements every second, reliable data can only be
346 achieved at intervals of around 30 seconds (exact values can be determined through future testing) due
347 to the residence time of aerosols in the nephelometer and potential light source instability. If four
348 nephelometers are available, a more advanced optical system can be designed (Fig. 3b) that does not
349 require switching between the interstitial inlet and the TSP inlet. Instead, two nephelometers would be
350 placed downstream of the interstitial inlet and two downstream of the TSP inlet, enabling higher time
351 resolution effective supersaturation measurements. Other types of optical instruments exist that can
352 achieve stable second-level aerosol scattering or extinction measurements with a stable laser light
353 source [Moise et al., 2015; Zhou et al., 2020]. Therefore, with the development of suitable optical
354 instruments, it may be possible to achieve second-level effective supersaturation measurements.

355 **4. Discussions on Limitations and Advantages**

356 The proposed theoretical framework enables simultaneous measurements of D_a and κ for
357 activated aerosols, leveraging the high time resolution of optical instruments to potentially provide
358 second-level measurements of supersaturation. However, several limitations should be discussed and
359 might be improved upon: **(1) Shape of size-resolved AR curve:** Cloud chamber studies have shown
360 that supersaturation fluctuations can lead to the coexistence of particles with the same critical
361 supersaturation as both interstitial aerosols and cloud droplets (Shawon et al., 2021). This results in
362 size-resolved AR curves deviate more from stepwise shape, a phenomenon also observed in some field
363 measurements (Henning et al., 2004; Mertes et al., 2007). Despite this, a critical diameter D_a still exists,
364 and such non-ideal curves can be treated a high standard deviation σ in the activation error function
365 (Eq. 2), which does not fundamentally undermine the proposed framework, however, should be further
366 checked for different cloud types. **(2) Measurement of κ :** Although the framework measures the
367 overall κ of activated aerosols, the κ needed for supersaturation calculations is that of aerosols near
368 D_a (κ_{D_a}). For $D_a > \sim 200$ nm, the derived $\kappa_{act,f(RH)}$ can provide a first-order estimate of κ_{D_a} , based on
369 observed size-dependent characteristics of κ values (Liu et al., 2014; Shen et al., 2021; Wang et al.,
370 2024), though more comprehensive evaluations are needed. Additionally, κ measured under

371 subsaturated conditions differs from that under supersaturated conditions (Tao et al., 2023) might also
372 bring some uncertainties. However, as shown in Fig. S1b, even a bias of 0.1 in κ only result in a $\sim 0.01\%$
373 bias when SS is $\sim 0.1\%$ and a $\sim 0.005\%$ bias when SS is $\sim 0.05\%$ in supersaturation retrievals, making
374 the first-order estimates of κ_{D_a} from optical measurements generally suitable for supersaturation
375 observations. **(3) Limitations in D_a Retrievals:** Current techniques using aerosol scattering
376 measurements at visible wavelengths (e.g., nephelometers) are reliable only for $D_a > 100$ nm as shown
377 in Fig. 1a, limiting effective supersaturation measurements to less than 0.21% (assuming a typical κ of
378 0.3). This restriction makes the technique most applicable to fog and stratus or stratocumulus cloud
379 measurements. However, incorporating scattering measurements at ultraviolet wavelengths could
380 improve sensitivity to smaller D_a and lower κ , enabling measurements in conditions with higher
381 effective supersaturation and a broader range of cloud types in the future.

382 The uncertainty in effective supersaturation observations using this framework primarily arises
383 from the uncertainties in deriving D_a and κ_{D_a} . The uncertainty in D_a observations using the Aurora
384 3000 nephelometer as the optical sensor under varying conditions is detailed in Fig. 1c. Factors
385 affecting the accuracy of κ_{D_a} include: (1) the size dependence of κ of activated aerosols; (2)
386 uncertainties related to surface tension, slightly soluble components, and other factors that lead to
387 differences in κ differences under subsaturated and supersaturated conditions. Based on previous
388 studies on the size dependence of κ (Peng et al., 2020) and the differences between subsaturated and
389 supersaturated conditions (Whitehead et al., 2014; Liu et al., 2018; Tao et al., 2023), a 50% uncertainty
390 (three times the standard deviation) was assumed in the derivation of κ_{D_a} for the uncertainty analysis.
391 Using this approach, the uncertainty in effective supersaturation measurements, estimated through the
392 Monte Carlo method, is shown in Fig. 4. The analysis indicates that applying this framework with the
393 Aurora 3000 nephelometer as the optical sensor results in an uncertainty of approximately 5%. The
394 precision of effective supersaturation measurements is directly linked to the accuracy of the optical
395 sensor's scattering signal. For example, the Aurora 3000 has an accuracy of 1 Mm^{-1} , which leads to
396 different levels of precision in D_a and hygroscopicity measurements depending on the scattering signal
397 strength. If the scattering signal from the total aerosol population is 100 Mm^{-1} , the precision of the
398 observed interstitial aerosol scattering fraction f_{sp} is about 1%. Based on the relationship between f_{sp}
399 and D_a shown in Fig. 1b, this leads to a precision of approximately 3 nm for D_a , which results in an
400 effective supersaturation precision of $\sim 0.01\%$ when supersaturation is near 0.2% , or $\sim 0.0002\%$ when
401 supersaturation is near 0.02% . However, if the scattering signal is lower (e.g., 10 Mm^{-1}), a bias of 1
402 Mm^{-1} could result in effective supersaturation bias to as much as $\sim 0.07\%$ when supersaturation is near

403 0.2%, making the measurements unreliable. In summary, while the proposed framework demonstrates
404 the feasibility of observing effective supersaturation with an advanced optical system, the accuracy

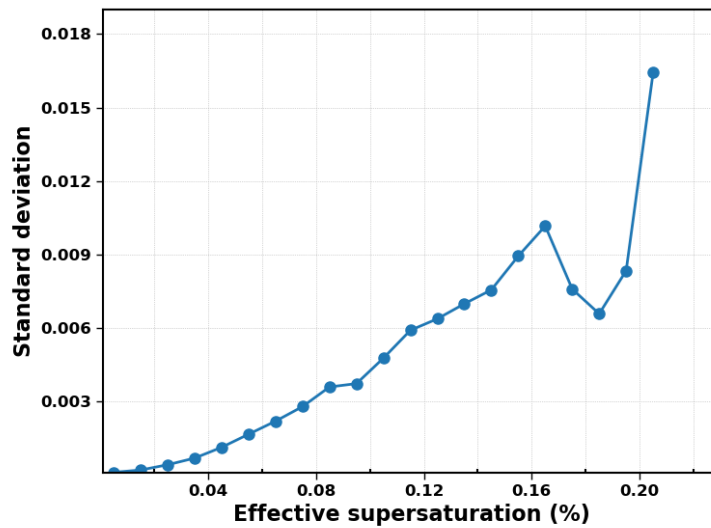


Figure 4. The standard deviations of effective supersaturations under different effective supersaturation (SS) levels.

405 and precision depend on the resolution of the optical sensors, the scattering parameters being measured,
406 and the scattering signal levels of aerosols in clouds. Enhancing the sensor precision to 0.1 Mm^{-1} or
407 even 0.01 Mm^{-1} , and incorporating ultraviolet wavelengths and multiple scattering angles, might
408 enable high-accuracy supersaturation measurements across a broad range of supersaturation conditions,
409 especially in cleaner environments.

410 As mentioned in Sect. 2.1, the theoretical framework proposed in this study is designed to observe
411 effective supersaturation fluctuations, rather than supersaturation fluctuations themselves. While there
412 are non-negligible uncertainties associated with observing effective supersaturation using the proposed
413 theory, the size and hygroscopicity distributions of total interstitial and activated aerosol populations
414 remain nearly constant when measured with second-scale or shorter time resolution. The parameter
415 that changes over time is the dynamic exchange between interstitial and activated aerosols.
416 Consequently, fluctuations in the scattering signals of interstitial and activated aerosols can reflect this
417 exchange at high temporal resolution. Since effective supersaturation fluctuations result from
418 underlying supersaturation variations, they could, in principle, provide insights into the causes of these
419 fluctuations, such as turbulence, though this would require further investigation and endeavor. In
420 addition, for size-resolved AR, both σ and MAF are crucial parameters. However, using scattering
421 coefficients at just three wavelengths of Aurora 3000 nephelometer is insufficient for accurately
422 retrieving σ and MAF. If σ and MAF could be measured more precisely through the extended optical
423 framework, it would provide deeper insights into supersaturation fluctuations.

424 Despite these limitations, the proposed theoretical framework represents the first system capable
425 of directly providing high time resolution measurements of effective supersaturations using a single
426 instrument. This system is particularly well-suited for surface fog and mountain cloud observations,
427 and when coupled with aerial vehicles, it could also be employed for measurements in aloft clouds.
428 The system offers several advantages for cloud and fog measurements: **(1) High-Resolution**
429 **Supersaturation Measurements:** The system can provide measurements of effective supersaturations
430 at even a second-level resolution, making it feasible for observing effective supersaturation
431 fluctuations and supporting investigations into fog and cloud evolution mechanisms. **(2) Long-Term**
432 **Measurement Capability:** The optical measurements, such as those from the nephelometer system,
433 are well-suited for long-term observations, making it possible to acquire climatological data on the
434 variability of fogs and mountain clouds. **(3) Comprehensive Aerosol and Cloud Data:** In addition to
435 measuring effective supersaturations, the system directly captures the scattering and hygroscopic
436 properties of both interstitial and activated aerosols. With further algorithm development, it could also
437 retrieve the number concentrations of available cloud condensation nuclei (CCN) at certain
438 supersaturations, as well as cloud droplet number concentrations, based on previous studies that have
439 observed CCN using optical methods (Tao et al., 2018a). **(4) Monitoring Aerosol Hygroscopic**
440 **Behavior:** The system continuously monitors aerosol hygroscopic behavior under subsaturated
441 conditions along with the corresponding optical properties. This allows for clear documentation of the
442 formation and dissipation of fog/cloud events, as well as the variation in aerosol optical and
443 hygroscopic properties. Overall, the datasets generated by this system are well-suited for in-depth
444 investigations of cloud physics and aerosol-cloud interactions. This system has the potential to
445 significantly advance fundamental research on clouds and fogs. However, further theoretical studies
446 are needed to refine and optimize this type of system.

447

448

449

450

451

452

453 **Financial Supports.** This work is supported by National Natural Science Foundation of China
454 (42175083, 42175127), and the Fundamental Research Funds for the Central Universities.

455

456 **Competing interests.** The authors declare that they have no conflict of interest.

457

458 **Data Availability.** All data presented in Figures of this manuscript are freely available at Kuang, Y.
459 (2024), and more specific data will be made available on request.

460

461 **Author contribution.** YK conceived the theoretical framework and wrote the manuscript. JT, HX, L
462 L, WX and WeX participated the field campaign and conducted measurements of aerosol chemical
463 and physical properties. YS, PL, CZ reviewed and commented on the paper.

464

465

466

467

468

469

470

471

472

473

474

475

476

477

478

479

480 **References**

- 481 Abade, G. C., Grabowski, W. W., and Pawlowska, H.: Broadening of Cloud Droplet Spectra through
482 Eddy Hopping: Turbulent Entraining Parcel Simulations, *Journal of the Atmospheric Sciences*, 75,
483 3365-3379, <https://doi.org/10.1175/JAS-D-18-0078.1>, 2018.
- 484 Abdul-Razzak, H., Ghan, S. J., and Rivera-Carpio, C.: A parameterization of aerosol activation: 1.
485 Single aerosol type, *Journal of Geophysical Research: Atmospheres*, 103, 6123-6131,
486 <https://doi.org/10.1029/97JD03735>, 1998.
- 487 Anderson, J. C., Beeler, P., Ovchinnikov, M., Cantrell, W., Krueger, S., Shaw, R. A., Yang, F., and
488 Fierce, L.: Enhancements in Cloud Condensation Nuclei Activity From Turbulent Fluctuations in
489 Supersaturation, *Geophysical Research Letters*, 50, e2022GL102635,
490 <https://doi.org/10.1029/2022GL102635>, 2023.
- 491 Chandrakar, K. K., Cantrell, W., Chang, K., Ciochetto, D., Niedermeier, D., Ovchinnikov, M., Shaw,
492 R. A., and Yang, F.: Aerosol indirect effect from turbulence-induced broadening of cloud-droplet size
493 distributions, *Proceedings of the National Academy of Sciences*, 113, 14243-14248,
494 doi:10.1073/pnas.1612686113, 2016.
- 495 Chandrakar, K. K., Cantrell, W., and Shaw, R. A.: Influence of Turbulent Fluctuations on Cloud
496 Droplet Size Dispersion and Aerosol Indirect Effects, *Journal of the Atmospheric Sciences*, 75, 3191-
497 3209, <https://doi.org/10.1175/JAS-D-18-0006.1>, 2018.
- 498 Chandrakar, K. K., Saito, I., Yang, F., Cantrell, W., Gotoh, T., and Shaw, R. A.: Droplet size
499 distributions in turbulent clouds: experimental evaluation of theoretical distributions, *Quarterly*
500 *Journal of the Royal Meteorological Society*, 146, 483-504, <https://doi.org/10.1002/qj.3692>, 2020.
- 501 Cooper, W. A.: Effects of Variable Droplet Growth Histories on Droplet Size Distributions. Part I:
502 Theory, *Journal of Atmospheric Sciences*, 46, 1301-1311, [https://doi.org/10.1175/1520-0469\(1989\)046<1301:EOVDGH>2.0.CO;2](https://doi.org/10.1175/1520-0469(1989)046<1301:EOVDGH>2.0.CO;2), 1989.
- 504 Davies, J. F., Zuend, A., and Wilson, K. R.: Technical note: The role of evolving surface tension in
505 the formation of cloud droplets, *Atmospheric Chemistry and Physics*, 19, 2933-2946, 10.5194/acp-19-
506 2933-2019, 2019.
- 507 Ditas, F., Shaw, R. A., Siebert, H., Simmel, M., Wehner, B., and Wiedensohler, A.: Aerosols-cloud
508 microphysics-thermodynamics-turbulence: evaluating supersaturation in a marine stratocumulus cloud,
509 *Atmospheric Chemistry and Physics*, 12, 2459-2468, 10.5194/acp-12-2459-2012, 2012.
- 510 Gérard, V., Nozière, B., Baduel, C., Fine, L., Frossard, A. A., and Cohen, R. C.: Anionic, Cationic,
511 and Nonionic Surfactants in Atmospheric Aerosols from the Baltic Coast at Askö, Sweden:
512 Implications for Cloud Droplet Activation, *Environmental science & technology*, 50, 2974-2982,
513 10.1021/acs.est.5b05809, 2016.
- 514 Gong, X., Wang, Y., Xie, H., Zhang, J., Lu, Z., Wood, R., Stratmann, F., Wex, H., Liu, X., and Wang,
515 J.: Maximum Supersaturation in the Marine Boundary Layer Clouds Over the North Atlantic, *AGU*
516 *Advances*, 4, e2022AV000855, <https://doi.org/10.1029/2022AV000855>, 2023.
- 517 Gussman, R. A., Kenny, L. C., Labickas, M., and Norton, P.: Design, Calibration, and Field Test of a
518 Cyclone for PM 1 Ambient Air Sampling, *Aerosol Science and Technology*, 36, 361-365,
519 10.1080/027868202753504461, 2002.
- 520 Hammer, E., Gysel, M., Roberts, G. C., Elias, T., Hofer, J., Hoyle, C. R., Bukowiecki, N., Dupont, J.
521 C., Burnet, F., Baltensperger, U., and Weingartner, E.: Size-dependent particle activation properties in
522 fog during the ParisFog 2012/13 field campaign, *Atmospheric Chemistry and Physics*, 14, 10517-
523 10533, 10.5194/acp-14-10517-2014, 2014.

524 Han, S., Hong, J., Luo, Q., Xu, H., Tan, H., Wang, Q., Tao, J., Zhou, Y., Peng, L., He, Y., Shi, J., Ma,
525 N., Cheng, Y., and Su, H.: Hygroscopicity of organic compounds as a function of organic functionality,
526 water solubility, molecular weight, and oxidation level, *Atmospheric Chemistry and Physics*, 22,
527 3985-4004, 10.5194/acp-22-3985-2022, 2022.

528 Henning, S., Bojinski, S., Diehl, K., Ghan, S., Nyeki, S., Weingartner, E., Wurzler, S., and
529 Baltensperger, U.: Aerosol partitioning in natural mixed-phase clouds, *Geophysical Research Letters*,
530 31, <https://doi.org/10.1029/2003GL019025>, 2004.

531 Ho, K. F., Lee, S. C., Ho, S. S. H., Kawamura, K., Tachibana, E., Cheng, Y., and Zhu, T.: Dicarboxylic
532 acids, ketocarboxylic acids, α -dicarbonyls, fatty acids, and benzoic acid in urban aerosols collected
533 during the 2006 Campaign of Air Quality Research in Beijing (CAREBeijing-2006), *Journal of*
534 *Geophysical Research: Atmospheres*, 115, <https://doi.org/10.1029/2009JD013304>, 2010.

535 Hudson, J. G., and Yum, S. S.: Droplet Spectral Broadening in Marine Stratus, *Journal of the*
536 *Atmospheric Sciences*, 54, 2642-2654, [https://doi.org/10.1175/1520-0469\(1997\)054<2642:DSBIMS>2.0.CO;2](https://doi.org/10.1175/1520-0469(1997)054<2642:DSBIMS>2.0.CO;2), 1997.

538 Hudson, J. G., Noble, S., and Jha, V.: Stratus cloud supersaturations, *Geophysical Research Letters*,
539 37, <https://doi.org/10.1029/2010GL045197>, 2010.

540 Kaufman, Y. J., and Tanré, D.: Effect of variations in super-saturation on the formation of cloud
541 condensation nuclei, *Nature*, 369, 45-48, 10.1038/369045a0, 1994.

542 Kuang, Y., Zhao, C., Tao, J., Bian, Y., Ma, N., and Zhao, G.: A novel method for deriving the aerosol
543 hygroscopicity parameter based only on measurements from a humidified nephelometer system,
544 *Atmospheric Chemistry and Physics*, 17, 6651-6662, 10.5194/acp-17-6651-2017, 2017.

545 Kuang, Y., Zhao, C. S., Zhao, G., Tao, J. C., Xu, W., Ma, N., and Bian, Y. X.: A novel method for
546 calculating ambient aerosol liquid water content based on measurements of a humidified nephelometer
547 system, *Atmospheric Measurement Techniques*, 11, 2967-2982, 10.5194/amt-11-2967-2018, 2018.

548 Kuang, Y., He, Y., Xu, W., Zhao, P., Cheng, Y., Zhao, G., Tao, J., Ma, N., Su, H., Zhang, Y., Sun, J.,
549 Cheng, P., Yang, W., Zhang, S., Wu, C., Sun, Y., and Zhao, C.: Distinct diurnal variation in organic
550 aerosol hygroscopicity and its relationship with oxygenated organic aerosol, *Atmospheric Chemistry*
551 *and Physics*, 20, 865-880, 10.5194/acp-20-865-2020, 2020.

552 Kuang, Y., Huang, S., Xue, B., Luo, B., Song, Q., Chen, W., Hu, W., Li, W., Zhao, P., Cai, M., Peng,
553 Y., Qi, J., Li, T., Wang, S., Chen, D., Yue, D., Yuan, B., and Shao, M.: Contrasting effects of secondary
554 organic aerosol formations on organic aerosol hygroscopicity, *Atmospheric Chemistry and Physics*,
555 21, 10375-10391, 10.5194/acp-21-10375-2021, 2021.

556 Kuang, Y., Xu, W., Tao, J., Luo, B., Liu, L., Xu, H., Xu, W., Xue, B., Zhai, M., Liu, P., and Sun, Y.:
557 Divergent Impacts of Biomass Burning and Fossil Fuel Combustion Aerosols on Fog-Cloud
558 Microphysics and Chemistry: Novel Insights From Advanced Aerosol-Fog Sampling, *Geophysical*
559 *Research Letters*, 51, e2023GL107147, <https://doi.org/10.1029/2023GL107147>, 2024.

560 Lee, W.-C., Deng, Y., Zhou, R., Itoh, M., Mochida, M., and Kuwata, M.: Water Solubility Distribution
561 of Organic Matter Accounts for the Discrepancy in Hygroscopicity among Sub- and Supersaturated
562 Humidity Regimes, *Environmental science & technology*, 10.1021/acs.est.2c04647, 2022.

563 Liu, H. J., Zhao, C. S., Nekat, B., Ma, N., Wiedensohler, A., van Pinxteren, D., Spindler, G., Müller,
564 K., and Herrmann, H.: Aerosol hygroscopicity derived from size-segregated chemical composition and
565 its parameterization in the North China Plain, *Atmospheric Chemistry and Physics*, 14, 2525-2539,
566 10.5194/acp-14-2525-2014, 2014.

567 Liu, P., Song, M., Zhao, T., Gunthe, S. S., Ham, S., He, Y., Qin, Y. M., Gong, Z., Amorim, J. C.,
568 Bertram, A. K., and Martin, S. T.: Resolving the mechanisms of hygroscopic growth and cloud
569 condensation nuclei activity for organic particulate matter, *Nature communications*, 9, 4076,
570 10.1038/s41467-018-06622-2, 2018.

571 Lu, C., Liu, Y., Yum, S. S., Chen, J., Zhu, L., Gao, S., Yin, Y., Jia, X., and Wang, Y.: Reconciling
572 Contrasting Relationships Between Relative Dispersion and Volume-Mean Radius of Cloud Droplet
573 Size Distributions, *Journal of Geophysical Research: Atmospheres*, 125, e2019JD031868,
574 <https://doi.org/10.1029/2019JD031868>, 2020.

575 Müller, T., Laborde, M., Kassell, G., and Wiedensohler, A.: Design and performance of a three-
576 wavelength LED-based total scatter and backscatter integrating nephelometer, *Atmospheric
577 Measurement Techniques*, 4, 1291-1303, 10.5194/amt-4-1291-2011, 2011.

578 Ma, N., Zhao, C. S., Nowak, A., Müller, T., Pfeifer, S., Cheng, Y. F., Deng, Z. Z., Liu, P. F., Xu, W.
579 Y., Ran, L., Yan, P., Göbel, T., Hallbauer, E., Mildenerger, K., Henning, S., Yu, J., Chen, L. L., Zhou,
580 X. J., Stratmann, F., and Wiedensohler, A.: Aerosol optical properties in the North China Plain during
581 HaChi campaign: an in-situ optical closure study, *Atmospheric Chemistry and Physics*, 11, 5959-5973,
582 10.5194/acp-11-5959-2011, 2011.

583 Mazoyer, M., Burnet, F., Denjean, C., Roberts, G. C., Haeffelin, M., Dupont, J. C., and Elias, T.:
584 Experimental study of the aerosol impact on fog microphysics, *Atmospheric Chemistry and Physics*,
585 19, 4323-4344, 10.5194/acp-19-4323-2019, 2019.

586 Mertes, S., Verheggen, B., Walter, S., Connolly, P., Ebert, M., Schneider, J., Bower, K. N., Cozic, J.,
587 Weinbruch, S., Baltensperger, U., and Weingartner, E.: Counterflow Virtual Impactor Based
588 Collection of Small Ice Particles in Mixed-Phase Clouds for the Physico-Chemical Characterization
589 of Tropospheric Ice Nuclei: Sampler Description and First Case Study, *Aerosol Science and
590 Technology*, 41, 848-864, 10.1080/02786820701501881, 2007.

591 Nozière, B., Ekström, S., Alsberg, T., and Holmström, S.: Radical-initiated formation of
592 organosulfates and surfactants in atmospheric aerosols, *Geophysical Research Letters*, 37,
593 <https://doi.org/10.1029/2009GL041683>, 2010.

594 Ovadnevaite, J., Zuend, A., Laaksonen, A., Sanchez, K. J., Roberts, G., Ceburnis, D., Decesari, S.,
595 Rinaldi, M., Hodas, N., Facchini, M. C., Seinfeld, J. H., and C, O. D.: Surface tension prevails over
596 solute effect in organic-influenced cloud droplet activation, *Nature*, 546, 637-641,
597 10.1038/nature22806, 2017.

598 Peng, C., Wang, Y., Wu, Z., Chen, L., Huang, R.-J., Wang, W., Wang, Z., Hu, W., Zhang, G., Ge, M.,
599 Hu, M., Wang, X., and Tang, M.: Tropospheric aerosol hygroscopicity in China, *Atmospheric
600 Chemistry and Physics*, 20, 13877-13903, 10.5194/acp-20-13877-2020, 2020.

601 Petters, M. D., and Kreidenweis, S. M.: A single parameter representation of hygroscopic growth and
602 cloud condensation nucleus activity, *Atmospheric Chemistry and Physics*, 7, 1961-1971, 2007.

603 Petters, M. D., and Kreidenweis, S. M.: A single parameter representation of hygroscopic growth and
604 cloud condensation nucleus activity - Part 2: Including solubility, *Atmospheric Chemistry and Physics*,
605 8, 6273-6279, 2008.

606 Petters, M. D., and Kreidenweis, S. M.: A single parameter representation of hygroscopic growth and
607 cloud condensation nucleus activity - Part 3: Including surfactant partitioning, *Atmospheric Chemistry
608 and Physics*, 13, 1081-1091, 10.5194/acp-13-1081-2013, 2013.

609 Prabhakaran, P., Shawon, A. S. M., Kinney, G., Thomas, S., Cantrell, W., and Shaw, R. A.: The role
610 of turbulent fluctuations in aerosol activation and cloud formation, *Proceedings of the National
611 Academy of Sciences*, 117, 16831-16838, 10.1073/pnas.2006426117, 2020.

612 Qiao, H., Kuang, Y., Yuan, F., Liu, L., Zhai, M., Xu, H., Zou, Y., Deng, T., and Deng, X.: Unlocking
613 the Mystery of Aerosol Phase Transitions Governed by Relative Humidity History Through an
614 Advanced Outdoor Nephelometer System, *Geophysical Research Letters*, 51, e2023GL107179,
615 <https://doi.org/10.1029/2023GL107179>, 2024.

616 Riipinen, I., Rastak, N., and Pandis, S. N.: Connecting the solubility and CCN activation of complex
617 organic aerosols: a theoretical study using solubility distributions, *Atmospheric Chemistry and Physics*,
618 15, 6305-6322, 10.5194/acp-15-6305-2015, 2015.

619 Rose, D., Gunthe, S. S., Mikhailov, E., Frank, G. P., Dusek, U., Andreae, M. O., and Pöschl, U.:
620 Calibration and measurement uncertainties of a continuous-flow cloud condensation nuclei counter
621 (DMT-CCNC): CCN activation of ammonium sulfate and sodium chloride aerosol particles in theory
622 and experiment, *Atmospheric Chemistry and Physics*, 8, 1153-1179, 10.5194/acp-8-1153-2008, 2008.

623 Saito, I., Gotoh, T., and Watanabe, T.: Broadening of Cloud Droplet Size Distributions by
624 Condensation in Turbulence, *Journal of the Meteorological Society of Japan. Ser. II*, 97, 867-891,
625 10.2151/jmsj.2019-049, 2019.

626 Saliba, G., Bell, D. M., Suski, K. J., Fast, J. D., Imre, D., Kulkarni, G., Mei, F., Mülmenstädt, J. H.,
627 Pekour, M., Shilling, J. E., Tomlinson, J., Varble, A. C., Wang, J., Thornton, J. A., and Zelenyuk, A.:
628 Aircraft measurements of single particle size and composition reveal aerosol size and mixing state
629 dictate their activation into cloud droplets, *Environmental Science: Atmospheres*, 3, 1352-1364,
630 10.1039/D3EA00052D, 2023.

631 Sanchez, K. J., Russell, L. M., Modini, R. L., Frossard, A. A., Ahlm, L., Corrigan, C. E., Roberts, G.
632 C., Hawkins, L. N., Schroder, J. C., Bertram, A. K., Zhao, R., Lee, A. K. Y., Lin, J. J., Nenes, A.,
633 Wang, Z., Wonauschütz, A., Sorooshian, A., Noone, K. J., Jonsson, H., Toom, D., Macdonald, A. M.,
634 Leaitch, W. R., and Seinfeld, J. H.: Meteorological and aerosol effects on marine cloud microphysical
635 properties, *Journal of Geophysical Research: Atmospheres*, 121, 4142-4161,
636 <https://doi.org/10.1002/2015JD024595>, 2016.

637 Sanchez, K. J., Roberts, G. C., Saliba, G., Russell, L. M., Twohy, C., Reeves, J. M., Humphries, R. S.,
638 Keywood, M. D., Ward, J. P., and McRobert, I. M.: Measurement report: Cloud processes and the
639 transport of biological emissions affect southern ocean particle and cloud condensation nuclei
640 concentrations, *Atmospheric Chemistry and Physics*, 21, 3427-3446, 10.5194/acp-21-3427-2021,
641 2021.

642 Sardina, G., Picano, F., Brandt, L., and Caballero, R.: Continuous Growth of Droplet Size Variance
643 due to Condensation in Turbulent Clouds, *Physical Review Letters*, 115, 184501,
644 10.1103/PhysRevLett.115.184501, 2015.

645 Seinfeld, J., and Pandis, S.: *Atmospheric Chemistry and Physics: From Air Pollution to Climate
646 Change*, Third Edition, 2016.

647 Seinfeld, J. H., Bretherton, C., Carslaw, K. S., Coe, H., DeMott, P. J., Dunlea, E. J., Feingold, G.,
648 Ghan, S., Guenther, A. B., Kahn, R., Kraucunas, I., Kreidenweis, S. M., Molina, M. J., Nenes, A.,
649 Penner, J. E., Prather, K. A., Ramanathan, V., Ramaswamy, V., Rasch, P. J., Ravishankara, A. R.,
650 Rosenfeld, D., Stephens, G., and Wood, R.: Improving our fundamental understanding of the role of
651 aerosol–cloud interactions in the climate system, *Proceedings of the National Academy of Sciences*,
652 113, 5781-5790, 10.1073/pnas.1514043113, 2016.

653 Shaw, R. A., Cantrell, W., Chen, S., Chuang, P., Donahue, N., Feingold, G., Kollias, P., Korolev, A.,
654 Kreidenweis, S., Krueger, S., Mellado, J. P., Niedermeier, D., and Xue, L.: Cloud–Aerosol–
655 Turbulence Interactions: Science Priorities and Concepts for a Large-Scale Laboratory Facility,
656 *Bulletin of the American Meteorological Society*, 101, E1026-E1035, <https://doi.org/10.1175/BAMS-D-20-0009.1>, 2020.

658 Shawon, A. S. M., Prabhakaran, P., Kinney, G., Shaw, R. A., and Cantrell, W.: Dependence of
659 Aerosol-Droplet Partitioning on Turbulence in a Laboratory Cloud, *Journal of Geophysical Research:*
660 *Atmospheres*, 126, e2020JD033799, <https://doi.org/10.1029/2020JD033799>, 2021.

661 Shen, C., Zhao, C., Ma, N., Tao, J., Zhao, G., Yu, Y., and Kuang, Y.: Method to Estimate Water Vapor
662 Supersaturation in the Ambient Activation Process Using Aerosol and Droplet Measurement Data,
663 *Journal of Geophysical Research: Atmospheres*, 0, 10.1029/2018JD028315, 2018.

664 Shen, C., Zhao, G., Zhao, W., Tian, P., and Zhao, C.: Measurement report: aerosol hygroscopic
665 properties extended to 600 nm in the urban environment, *Atmospheric Chemistry and Physics*,
666 21, 1375-1388, 10.5194/acp-21-1375-2021, 2021.

667 Siebert, H., and Shaw, R. A.: Supersaturation Fluctuations during the Early Stage of Cumulus
668 Formation, *Journal of the Atmospheric Sciences*, 74, 975-988, <https://doi.org/10.1175/JAS-D-16-0115.1>, 2017.

670 Tao, J., Zhao, C., Kuang, Y., Zhao, G., Shen, C., Yu, Y., Bian, Y., and Xu, W.: A new method for
671 calculating number concentrations of cloud condensation nuclei based on measurements of a three-
672 wavelength humidified nephelometer system, *Atmospheric Measurement Techniques*, 11, 895-906,
673 10.5194/amt-11-895-2018, 2018a.

674 Tao, J., Zhao, C., Ma, N., and Kuang, Y.: Consistency and applicability of parameterization schemes
675 for the size-resolved aerosol activation ratio based on field measurements in the North China Plain,
676 *Atmospheric Environment*, 173, 316-324, <https://doi.org/10.1016/j.atmosenv.2017.11.021>, 2018b.

677 Tao, J., Kuang, Y., Luo, B., Liu, L., Xu, H., Ma, N., Liu, P., Xue, B., Zhai, M., Xu, W., Xu, W., and
678 Sun, Y.: Kinetic Limitations Affect Cloud Condensation Nuclei Activity Measurements Under Low
679 Supersaturation, *Geophysical Research Letters*, 50, e2022GL101603,
680 <https://doi.org/10.1029/2022GL101603>, 2023.

681 Wainwright, C., Chang, R. Y.-W., and Richter, D.: Aerosol Activation in Radiation Fog at the
682 Atmospheric Radiation Program Southern Great Plains Site, *Journal of Geophysical Research:*
683 *Atmospheres*, 126, e2021JD035358, <https://doi.org/10.1029/2021JD035358>, 2021.

684 Wang, J., Shilling, J. E., Liu, J., Zelenyuk, A., Bell, D. M., Petters, M. D., Thalman, R., Mei, F., Zaveri,
685 R. A., and Zheng, G.: Cloud droplet activation of secondary organic aerosol is mainly controlled by
686 molecular weight, not water solubility, *Atmospheric Chemistry and Physics*, 19, 941-954,
687 10.5194/acp-19-941-2019, 2019.

688 Wang, Y., Li, J., Fang, F., Zhang, P., He, J., Pöhlker, M. L., Henning, S., Tang, C., Jia, H., Wang, Y.,
689 Jian, B., Shi, J., and Huang, J.: In-situ observations reveal weak hygroscopicity in the Southern Tibetan
690 Plateau: implications for aerosol activation and indirect effects, *npj Climate and Atmospheric Science*,
691 7, 77, 10.1038/s41612-024-00629-x, 2024.

692 Whitehead, J. D., Irwin, M., Allan, J. D., Good, N., and McFiggans, G.: A meta-analysis of particle
693 water uptake reconciliation studies, *Atmospheric Chemistry and Physics*, 14, 11833-11841,
694 10.5194/acp-14-11833-2014, 2014.

695 Yang, F., McGraw, R., Luke, E. P., Zhang, D., Kollias, P., and Vogelmann, A. M.: A new approach
696 to estimate supersaturation fluctuations in stratocumulus cloud using ground-based remote-sensing
697 measurements, *Atmospheric Measurement Techniques*, 12, 5817-5828, 10.5194/amt-12-5817-2019,
698 2019.

699 Yum, S. S., Hudson, J. G., and Xie, Y.: Comparisons of cloud microphysics with cloud condensation
700 nuclei spectra over the summertime Southern Ocean, *Journal of Geophysical Research: Atmospheres*,
701 103, 16625-16636, <https://doi.org/10.1029/98JD01513>, 1998.

702 Zíková, N., Pokorná, P., Makeš, O., Sedlák, P., Pešice, P., and Ždímal, V.: Activation of atmospheric
703 aerosols in fog and low clouds, *Atmospheric Environment*, 230, 117490,
704 <https://doi.org/10.1016/j.atmosenv.2020.117490>, 2020.

705